**Journal of Nuclear Medicine, published on November 25, 2015 as doi:10.2967/jnumed.115.160168**

# Feasibility of $^{18}$F-fluoromisonidazole kinetic modeling in head and neck cancer using shortened acquisition times

Milan Grkovski[1], Jazmin Schwartz[1], Mithat Gönen[2], Heiko Schöder[3], Nancy Y. Lee[4], Sean D. Carlin[3], Pat B. Zanzonico[1], John L. Humm[1], and Sadek A. Nehmeh[1]

[1]Department of Medical Physics, Memorial Sloan Kettering Cancer Center, New York, New York

[2]Department of Epidemiology-Biostatistics, Memorial Sloan Kettering Cancer Center, New York, New York

[3]Department of Radiology, Memorial Sloan Kettering Cancer Center, New York, New York

[4]Department of Radiation Oncology, Memorial Sloan Kettering Cancer Center, New York, New York

Corresponding Author:

Milan Grkovski, PhD

Department of Medical Physics

Memorial Sloan Kettering Cancer Center

1275 York Avenue

New York, NY 10065

Phone: 212-639-2480

FAX: 212-717-3010

Email: grkovskm@mkscc.org

Word count: 5898

Running Title: Shortened FMISO dynamic PET

## ABSTRACT

$^{18}$F-fluoromisonidazole dynamic positron emission tomography (dPET) is used to identify tumor hypoxia non-invasively. Its routine clinical implementation, however, has been hampered by the long acquisition times required. We investigated the feasibility of kinetic modeling using shortened acquisition times in $^{18}$F-fluoromisonidazole dPET, with the goal of expediting the clinical implementation of $^{18}$F-fluoromisonidazole dPET protocols.

**Methods**: Six patients with squamous cell carcinoma of the head and neck and ten HT29 colorectal carcinoma-bearing nude rats were studied. In addition to an $^{18}$F-fluorodeoxyglucose PET scan, each patient underwent a 45-min $^{18}$F-fluoromisonidazole dPET scan, followed by 10 min acquisitions at 96±4 and 163±17 min post-injection. Ninety-minute $^{18}$F-fluoromisonidazole dPET acquisitions were performed in animals. Intra-tumor voxels were classified into 4 clusters based on their kinetic behavior using k-means clustering. Kinetic modeling was carried out using the foregoing full datasets (FD) and repeated for each of two shortened datasets corresponding to the first ~100 min (SD1; patients only) or the first 45 min (SD2) of dPET data. The kinetic rate constants (KRCs) as calculated with a 2-compartment model for both SD1 and SD2 were compared to those derived from FD by correlation (Pearson), regression (Passing-Bablok), deviation (Bland-Altman) and classification (area under receiver operating characteristic curve; AUC) analyses. Simulations were performed to assess uncertainties due to statistical noise.

**Results**: Strong correlation ($r \geq 0.75$, $p < 0.001$) existed between all KRCs deduced from both SD1 and SD2, and from FD. Significant differences between KRCs were only found for FD-SD2 correlations in patient studies. $K_1$ and $k_3$ were reproducible to within ~6% and ~30% (FD-SD1; patients) and ~4% and ~75% (FD-SD2; animals). AUC values for

classification of patient clusters as hypoxic, using a tumor-to-blood ratio>1.2, were 0.91 (SD1) and 0.86 (SD2). The percentage standard deviation in estimating $K_1$ and $k_3$ from 45-min shortened datasets due to noise was <1% and between 2-12% respectively.

**Conclusion**: Using single-session 45-min shortened $^{18}$F-fluoromisonidazole dynamic PET datasets appears to be adequate for the identification of intra-tumor regions of hypoxia. However, $k_3$ was significantly overestimated in the clinical cohort. Further studies are necessary to evaluate the clinical significance of differences between the results as calculated from full and shortened datasets.

**Key words**: Dynamic PET; hypoxia; $^{18}$F-fluoromisonidazole; kinetic modeling;

## INTRODUCTION

The relationship between tumor hypoxia and poor overall outcome has been demonstrated for several types of human malignancies (*1*), including head and neck cancer (*2-4*). Tumor hypoxia can be identified by measuring partial pressure of oxygen using polarographic electrodes (*3,5*). Another method to characterize tumor hypoxia is by means of immunohistochemical analysis of exogenous (e.g. pimonidazole, etanidazole pentafluoride) or endogenous (e.g. carbonic anhydrase IX, Hypoxia-inducible factor 1α) hypoxia markers (*6*). Both techniques, however, are invasive, require lesions accessible to needle placement and are subject to undersampling.

Positron emission tomography (PET) with $^{18}$F-fluoromisonidazole is a non-invasive imaging technique that has been shown to be clinically feasible for detecting tumor hypoxia (*7,8*). $^{18}$F-fluoromisonidazole passively diffuses out of the vasculature and through cell membranes due to its lipophilicity, and is reduced to a non-diffusible charged form by intracellular nitroreductases (*7*). Under normoxic conditions, the reduced form of fluoromisonidazole is rapidly oxidized back to its diffusible form, with tissue levels rapidly declining as blood-borne fluoromisonidazole is cleared. Otherwise, the fluoromisonidazole metabolites remain trapped and undergo irreversible reductions to form covalent bonds to macromolecules, leading to progressive accumulation of $^{18}$F within hypoxic cells (*7*). Previous studies suggested a tumor-to-blood ratio (TBR) in excess of 1.4 at 2+ hours post-injection (pi) to identify hypoxic volumes (*7,8*). However, a combination of severely hypoxic and necrotic tissues supplied by structurally and functionally abnormal vasculature may lead to low total uptake even at late time points. Conversely, the physiologic clearance of $^{18}$F-fluoromisonidazole from well-perfused normoxic tissue may result in measured activity concentrations comparable to those in

hypoxic tumors (*9,10*). To overcome the foregoing limitations in the interpretation of static $^{18}$F-fluoromisonidazole images, kinetic modeling of dynamic PET (dPET) data has been suggested as a means of reliably characterizing perfusion and identifying hypoxia in tumors (*9,10*).

A major drawback of such an approach are the long acquisition times typically used to extract the pharmacokinetic parameters of $^{18}$F-fluoromisonidazole. At our institution, the $^{18}$F-fluoromisonidazole dPET protocol consists of 30-45 min dPET followed by 10-min static PET acquisitions at ~90 min and at ~150-180 min post-injection (pi). Such lengthy protocols compromise clinical practicality as well as patient compliance and accrual. The aim of the current study was to assess the reproducibility of kinetic rate constants (KRCs) as calculated from shortened $^{18}$F-fluoromisonidazole dPET datasets, in (i) a cohort of patients with squamous cell carcinoma of the head and neck (SCCHN) and (ii) a preclinical rodent model. Special attention was paid to kinetic rate constants serving as surrogate metrics of perfusion ($K_1$) and hypoxia ($k_3$).

## MATERIALS AND METHODS

### Clinical Studies

This retrospective study was approved by our Institutional Review Board (IRB 04-070; registered under www.clinicaltrials.gov identifier NCT00606294) and all subjects signed a written informed consent regarding the examination and use of anonymous data for research and publication purposes. Patients aged 18+ years with a histologically confirmed diagnosis of SCCHN were eligible for this study. Exclusion criteria included all nasopharyngeal, paranasal sinus, salivary cancer, and thyroid malignancies, prior chemotherapy or radiotherapy within the last three years, previous surgical resection for the same disease, any prior radiotherapy to the head and neck region, and pregnancy.

Six male patients (59±10 yrs) were included in the study (Table 1). All patients were scanned on a flat-top couch insert in a radiotherapy treatment immobilization mask. Intravenous lines in contralateral antecubital veins were inserted for each patient and were used for radiotracer injection.

*$^{18}$F-fluorodeoxyglucose PET/CT Protocol.* Each patient underwent a baseline $^{18}$F-fluorodeoxyglucose PET/CT study for radiotherapy simulation. Patients were injected intravenously with 451±18 MBq of $^{18}$F-fluorodeoxyglucose (range, 437-477 MBq), after a fasting period of ≥6 hours. Whole body PET scans were acquired for 3 min per bed position, 70 cm field of view (FOV), starting at 69±10 min (range, 61-84 min) pi. Data were acquired on a General Electric Discovery STE PET/CT scanner (GE Health Care Inc.), having a resolution of ~5.5-mm full-width at half-maximum (FHWM) at the center of the FOV. The CT images were acquired with oral contrast using the following settings: 140 kVp, 250 mA, and 3.8-mm slice thickness. PET emission data were corrected for

attenuation, scatter, and random events, and then iteratively reconstructed into a 256×256×47 matrix (voxel dimensions: 2.73×2.73×3.27 $mm^3$) using the ordered subset expectation maximization algorithm provided by the manufacturer (2 iterations, 20 subsets, and a Gaussian post-filter of 6.0-mm FWHM).

*$^{18}$F-fluoromisonidazole PET/CT Protocol.* Each patient underwent $^{18}$F-fluoromisonidazole dPET imaging on a Discovery STE PET/CT scanner 1-3 days following the $^{18}$F- fluorodeoxyglucose PET/CT. $^{18}$F-fluoromisonidazole was prepared as previously reported (*11*). Patients received an intravenous bolus injection of 429±41 MBq of $^{18}$F-fluoromisonidazole (range, 364-475 MBq). The dPET acquisition was initiated simultaneously with the injection. $^{18}$F-fluoromisonidazole data were acquired in list-mode for one bed position, centered over the lesion, for 45 min (binned into 6×30-sec, 7×60-sec, and 7×300-sec frames). Two additional 10-min static image sets were acquired at 96±4 min (range, 90-103 min) and 163±17 (range, 150-186 min) pi. Patients were allowed a rest period between scans. Prior to each PET scan, a low-dose CT scan was performed for attenuation correction and image registration purposes; CT scans were performed with 120 kVp, 3.8-mm slice thickness, and 40 mA, 10 mA, and 80 mA for the first, second and third scans, respectively. List-mode PET data of the first 3 min of the dataset was retrospectively re-binned into 36×5-sec frames in order to delineate the carotid artery from the internal jugular vein and thereby define the input function (IF) volume of interest (VOI). All $^{18}$F-fluoromisonidazole PET images were reconstructed using the same parameters as for the $^{18}$F-fluorodeoxyglucose study.

**Preclinical Studies**

All animal experiments and procedures were approved by our Institutional Animal Care and Use Committee and complied with the National Institutes of Health regulations on the research use of rodents.

A total of 10 rats were included in this study. HT29 human colorectal carcinoma cells (ATCC Number HTB-38) were maintained in Dulbecco's Modified Eagle Medium (MediaTech Inc.) supplemented with 10% fetal bovine serum and 1% penicillin-streptomycin at 37°C in a 5% $CO_2$ atmosphere. Xenografts were initiated by subcutaneous injection of ~$5.0\times10^6$ cells in 0.2 mL of phosphate-buffered saline into the right hind limb of each of ten 6- to 8-week-old female athymic nu/nu rats as previously described (*12*). Animals (weight: 228±18g) were anesthetized by using 2% isoflurane in air. An activity of 41.3±2.9 MBq (range, 36.7-46.0 MBq) of $^{18}$F-fluoromisonidazole was administered via tail vein injection. Image acquisition was performed with either an R4 or Focus 120 microPET scanner (Siemens Medical Solutions Inc.), with animals in the prone position and the FOV centered on the tumor, using a 350- to 700-keV energy window and 6-ns coincidence timing window. Data were acquired in dynamic mode for a total of 90 min and binned into 4×5-, 4×10-, 4×30-, 7×60-, 10×300-, and 3×600-sec frames. Images were reconstructed using a 3D maximum a posteriori estimation algorithm into a 128×128×95 matrix (voxel dimensions 0.87×0.87×0.79 $mm^3$). The reconstructed image resolution was ~1.6 mm FWHM at the center of the FOV. Measurements performed with a uniformly filled phantom of comparable dimensions to a rat demonstrated adequate uniformity without attenuation and scatter correction. Therefore, no attenuation or scatter correction was applied for the rat image data.

**Image Analysis**

Reconstructed dPET images were analyzed with PMOD v3.504 (PMOD Technologies GmbH). For patient studies, eight lesions were identified on the $^{18}$F-fluorodeoxyglucose PET/CT scans. In one case (patient #5), dynamic $^{18}$F-fluoromisonidazole acquisition was interrupted at 40 min pi due to patient's discomfort and inability to continue. The two delayed $^{18}$F-fluoromisonidazole and the $^{18}$F-fluorodeoxyglucose image sets were spatially registered to the first $^{18}$F-fluoromisonidazole image set using the General Registration tool in GE AW Workstation v4.6. Rigid image registration was performed locally for each lesion using the CT image sets, and the resulting transformation matrices were applied to the corresponding PET image sets. The whole-tumor volume of interest (wVOI) was delineated on $^{18}$F-fluorodeoxyglucose images using a 50% of the maximum tumor activity concentration threshold and the resulting VOI was copied to the corresponding dynamic $^{18}$F-fluoromisonidazole image set. For animal studies, the wVOI was delineated manually on a slice-by-slice basis using the final frame (80-90 min).

**Kinetic Modeling**

Kinetic modeling of $^{18}$F-fluoromisonidazole dPET images was carried out in PMOD, using an irreversible one-plasma two-tissue compartment model (*13*). In this model, $C_p(t)$, $C_1(t)$ and $C_2(t)$ correspond to the activity concentration as a function of time pi in the plasma ($C_P$), in the form of free and otherwise non-hypoxia-localized activity in tissue ($C_1$), and in the form of hypoxia-localized tracer ($C_2$). The 4 unknowns estimated are: (1) $v_B$, the fractional vascular volume, (2) $K_1$, the transfer rate constant from $C_P$ to $C_1$, (3) $K_1/k_2$, the distribution volume of $C_1$, and (4) $k_3$, the rate of conversion from $C_1$ to $C_2$. $k_4$ was set to 0, assuming irreversible trapping of $^{18}$F-fluoromisonidazole (*7*). While $v_B$ and $K_1/k_2$ are unitless, $K_1$ and $k_3$ (assuming unit density tissue) are expressed in $min^{-1}$.

For patient studies, the input function was derived by segmenting the common carotid artery on the re-binned dPET dataset (i.e. corresponding to the 36×5-sec time frames). In two cases (patients #4 and #6), the list-mode data were not available; as the common carotid artery could not be identified from the original dPET dataset, the IF VOI was defined on the internal jugular vein. For animal studies, the input function was derived by segmenting the descending aorta (identified from a summed image of the first three frames (15 sec) of the study). All IF time activity curves (TACs) were corrected for partial volume effect by calculating the geometric transfer matrix containing weighting elements $w_{i,j}$ that represent the fraction of true activity spilled over from $VOI_i$ into $VOI_j$ (*14*). Neighboring regions were defined using k-means clustering based on the time-weighted Euclidean distance between the voxel TACs (10 clusters, 200 iterations) (*15*).

Voxels within each wVOI were similarly sub-classified into 4 clusters, with k-means clustering performed based on the first 45 min of dPET data. The choice of 4 tumor sub-volumes (cVOIs) was made to conceptually represent hypoxic, partially hypoxic, normoxic, and necrotic regions of the tumor. The Levenberg-Marquardt algorithm (*16*) was used to fit the cVOI-derived TACs to estimate the KRCs (100 random fits, 200 iterations). The target activity concentration at each time frame was weighed by (*13*)

$$w_i = \frac{1}{\sigma_i^2}, \quad \sigma_i = c\sqrt{\left(\frac{AC(t_i)}{\Delta t_i \times e^{-\lambda t_i}}\right)}, \tag{1}$$

where c is the scaling factor, $\Delta t_i$ is the frame duration, $AC(t_i)$ is the decay-corrected activity concentration measured at the mid-frame time $t_i$, and $\lambda=\ln 2/T_{1/2}$ is the isotope decay constant. Kinetic modeling was conducted for (i) the full dataset (FD; reference standard), (ii) the first ~100 min of dPET data (SD1; patients only), and (iii) the first 45 min of dPET data (SD2). The input function TACs that were corrected for partial volume

effect were fitted with a 3-term exponential function, using the available temporal data in each case, to obtain a modeled IF as

$$IF(t) = \begin{cases} Linear\ interpolation & t < t_0 \\ \sum_{i=1}^{3} A_i e^{-(t-t_0)\ln 2/T_i} & t \geq t_0 \end{cases}, \quad (2)$$

where IF(t) is the modeled activity concentration in the blood at time *t*, $t_0$ defines at what time the model switches from linear to tri-exponential interpolation between measured values (after the IF peak), while $A_i$ and $T_i$ terms represent the fitting parameters.

**Statistical Analysis**

The kinetic rate constants calculated from each of the two shortened datasets were compared to those derived from the full dataset in a stepwise approach. First, Pearson correlation coefficient (*r)* was computed to calculate the strength and direction of a linear relationship between the KRCs, modeled as

$$Y = \alpha + \beta X + \varepsilon, \quad (3)$$

where intercept $\alpha$, slope $\beta$, and $\varepsilon$ correspond to the systematic, proportional, and random differences. If a strong significant correlation ($r \geq 0.75$, $p < 0.05$) was found, non-parametric Passing-Bablok regression (*17*) was performed to test for the presence of systematic (95% confidence interval (95CI) for $\alpha$ does not include 0) and/or proportional (95CI for $\beta$ does not include 1) differences between the two sets of KRCs. A cumulative sum (Cusum) test for linearity was used to validate the applicability of Passing-Bablok analysis (*17*). Random differences between two sets of KRCs were measured using residual standard deviation (RSD). If the slope and intercept were not significantly different than 1 and 0, respectively, Bland-Altman analysis (*18*) was performed to calculate the 95% limits

of agreement, after testing for the normality assumption on the differences between two sets of KRCs using the Kolmogorov–Smirnov test.

Receiver operating characteristics analysis (*19*) was performed in patient studies to evaluate the reliability of shortened datasets for the task of identifying tumor hypoxia, using TBR>1.2 (*4*) as a discrimination threshold. The diagnostic performance was assessed based on $k_3$ and $K_i$ (influx rate constant, defined as $k_1k_3/(k_2+k_3)$, in units of $min^{-1}$) calculated from shortened datasets, and the area under the receiver operating characteristics curve (AUC) was subsequently determined (*19*). All statistical analyses were carried out in MedCalc v15.6 (MedCalc Software bvba).

**Simulations**

Modeled time activity curves (mTAC) were obtained by fitting all 32 cVOI-derived TACs from patients. For each mTAC, 100 samples of noisy TACs were simulated by adding noise consistent to that observed on a cluster level. The noise was estimated as follows: data were acquired on Discovery STE PET-CT using NEMA (National Electrical Manufacturers Association) IEC (International Electrotechnical Comission) body phantom filled with $^{18}$F-fluorodeoxyglucose (activity concentration was equivalent to the average tumor $^{18}$F-fluoromisonidazole activity concentration in the ~170-min time point), for 30 min in gated mode (10 bins), as described previously (*20*). Images were reconstructed using same parameters as in clinical studies. Fifty non-overlapping VOIs of 5×5×5 voxels (corresponding in size to the average patients´ cluster volumes) were drawn on the central axial plane in the phantom image set. For each VOI, a histogram of the average activity concentrations from the 10 gated image bins was constructed and fitted with a normal distribution fit, to calculate the standard deviation of the distribution and deduce the corresponding scaling factor *c* (as per Equation 1). The average scaling factor over

50 VOIs was subsequently used to simulate cluster noise on a frame-by-frame basis for each mTAC. Kinetic modeling was conducted using mTACs and input functions as derived from full datasets ($mTAC_{FD}$ and $IF_{FD}$; i.e. for SD1 and SD2, $mTAC_{FD}$ and $IF_{FD}$ were truncated). The percentage bias and percentage standard deviation were calculated with respect to the true value for each kinetic parameter (*13*):

$$\%bias_i = \left(\frac{\mu_{x_i}}{x_i^{true}} - 1\right) * 100, \quad (4)$$

$$\%stddev_i = \left(\frac{\sigma_{x_i}}{x_i^{true}}\right) * 100, \quad (5)$$

where $\mu_{x_i}$, $\sigma_{x_i}$, and $x_i^{true}$ are the sample mean, sample standard deviation, and true value of a kinetic parameter *x* for *i*-th cluster. Additionally, Pearson's *r* was calculated for $K_1$ and $k_3$ deduced from the 100 noisy TACs using FD and, SD1 and SD2 respectively.

## RESULTS

### Clinical Studies

Coronal images for patient #1 are shown in Figures 1-a ($^{18}$F-fluorodeoxyglucose PET) and 1-b ($^{18}$F-fluoromisonidazole PET). The corresponding IF and tumor TACs are shown in Figures 1-c and 1-d, respectively.

Clusters included 25.0±9.1% of tumor voxels (range, 7.9-46.0%). The KRCs calculated from the full dataset were 0.0032±0.0015 $min^{-1}$ (range, 0.00071-0.0078 $min^{-1}$) for $k_3$ and 0.33±0.13 $min^{-1}$ (range, 0.13-0.62 $min^{-1}$) for $K_1$. Subsequently, only clusters that resulted in $k_3$>0.001 $min^{-1}$ (i.e. greater than the value reported for normoxic tumors and normal tissue in head and neck (*13*)) were included in the analysis, a total of 29 (26) clusters for SD1 (SD2). The results of correlation, Passing-Bablok and Bland-Altman analyses are summarized in Figure 2 (FD-SD1), Figure 3 (FD-SD2), and in Table 2. Strong correlation ($r \geq 0.75$, $p<0.001$) was observed between all corresponding KRCs. Passing-Bablok regression for FD-SD1 correlations showed no significant biases. Bland-Altman analysis revealed <1% and <10% mean differences between the calculated $K_1$ and $k_3$ respectively, which were reproducible to within ~6% and ~30%. However, as proportional bias was observed when comparing FD-SD2, Bland-Altman analysis was not conducted. The analysis was repeated for $K_i$ (data not shown), and no significant biases were identified.

The AUC values for the classification of cVOIs as hypoxic are given in Table 3. Pearson's *r* between TBR and, $k_3$ and $K_i$ as calculated using FD, were 0.71 and 0.90 respectively ($p<0.001$). For classification analyses, all 32 clusters were included.

### Preclinical Studies

Coronal image for animal #1 (lesion #1) is shown in Figure 4-a, while the IF and TACs are shown in Figures 4-b and 4-c, respectively. The discontinuities in the example clusters may be due to noise propagated by the image reconstruction.

Clusters included 25.0±9.7% of tumor voxels (range, 7.4-44.2%). A total of 21 clusters were included in the analysis (excluding those for which $k_3$=0). The KRCs calculated from the FD were 0.0040±0.0026 $min^{-1}$ (range, 0.00041-0.0089 $min^{-1}$) for $k_3$ and 0.22±0.076 $min^{-1}$ (range, 0.085-0.35 $min^{-1}$) for $K_1$. The results of correlation, Passing-Bablok and Bland-Altman analyses are summarized in Figure 5 and Table 2. Strong correlation was observed in all cases. Passing-Bablok analysis revealed no proportional or systematic biases. Bland-Altman analysis revealed <1% and <25% mean differences between the calculated $K_1$ and $k_3$ respectively, which were reproducible to within ~4% and ~75%.

Correction factors to the input function due to partial volume effect for pooled data from both clinical and preclinical studies are shown in Figure 6. Correction factor is higher at initial times post-injection due to largest differences between activity concentrations of $^{18}$F-fluoromisonidazole in vasculature and surrounding tissue, falling to ~1 as $^{18}$F-fluoromisonidazole diffuses from the vasculature.

**Simulations**

The average scaling factor *c* over the 50 VOIs was 0.064±0.026. While no bias was observed, the %stddev in $k_3$ increased for shorter acquisition times and was inversely proportional to the true value of $k_3$, ranging from ~1-4%, ~1-6% and ~2-12% for FD, SD1 and SD2 respectively (Figure 7). For $K_1$, both %bias and %stddev were <1% in all cases. Correlation between $K_1$ as calculated using full and shortened noisy TACs was strong

($r$>0.90), while for $k_3$ it was lower ($r$=0.55 for SD1 and $r$=0.19 for SD2). Summary of simulation results is given in Table 4.

## DISCUSSION

Dynamic PET studies are largely confined to research applications, as the routine acquisition of multi-session dPET scans is challenging. Despite reports that additional prognostic information such as the composite assessment of hypoxia and blood flow can be obtained from the analysis of $^{18}$F-fluoromisonidazole dynamic PET data (*21,22*), static acquisitions at between 2-4 h post-injection are predominantly utilized (*23*). We investigated the feasibility of kinetic modeling of $^{18}$F-fluoromisonidazole dPET using shortened acquisition times as a means of overcoming the limitations of both static and dynamic $^{18}$F-fluoromisonidazole imaging in identifying regions of tumor hypoxia in a clinically practical manner.

Measured uptake values on a voxel level exhibit considerable variations that represent not only differences in metabolic processes, but also noise, which is propagated through image reconstruction and kinetic modeling (*10*). Misregistration between the three $^{18}$F-fluoromisonidazole scans may additionally compromise the accuracy of voxelwise kinetic modeling. Clustering was performed to reduce these effects, while maintaining the ability to study hypoxia and perfusion characteristics of tumor sub-volumes.

Strong correlations were found between all corresponding KRCs as calculated using shortened and full datasets (Table 2). In the clinical studies, Passing-Bablok regression revealed no significant differences between the KRCs as calculated from the FD and SD1, implying that using the ~100-min shortened datasets would not result in a bias in the estimation of KRCs. However, proportional differences were observed for FD-SD2 correlations. An increased RSD with larger 95% CIs was also measured, showing that kinetic modeling of $^{18}$F-fluoromisonidazole dPET in SCCHN patients will be more prone to errors in determining the KRCs as the duration of the study is further shortened. In

contrast, the results from the animal studies revealed no significant differences in the KRCs calculated from SD2 datasets. Narrower 95% CIs for slope, intercept and RSD were observed for KRCs calculated from the 45-min datasets in the animal compared to patient studies.

Results indicate that $k_3$ was overestimated when using shortened datasets. Analyzing kinetically heterogeneous regions with a compartment model designed for homogeneous tissues may result in the overestimation of $k_3$, the magnitude of which depends on the acquisition period (*24,25*). While this effect has been observed previously (*26-28*), further investigations are necessary to understand its significance in the context of $^{18}$F-fluoromisonidazole dPET.

Causes for the differences in the results between patient and animal studies may be attributed to a variety of factors including: the more rapid circulation time and metabolism in rodents compared to man, dissimilarity of pharmacokinetic characteristics of $^{18}$F-fluoromisonidazole in the two tumor types, different acquisition lengths for full datasets, the fact that the animals were anesthetized during the acquisition whereas the patients were not, and the increased uncertainty brought about by the need to co-register the piecewise acquisition in human studies. Additionally, list-mode PET data were not available for two patients. 30-sec initial time frames were therefore used, resulting in a lower peak activity concentration of the IF, leading to less stable KRC estimates (*13*).

The AUC, calculated to assess the reliability of shortened $^{18}$F-fluoromisonidazole dPET datasets for the task of identifying tumor hypoxia, was high when using either $k_3$ (0.80) or $K_i$ (0.86) values as calculated from 45-min dataset. These results suggest that single-session 45-min acquisitions in SCCHN patients may present an attractive alternative when utilized for identifying the presence of hypoxia on a tumor sub-volume level.

Simulations were performed to assess uncertainties in $^{18}$F-fluoromisonidazole kinetic modeling due to statistical noise and shortened acquisition time. The decrease in %stddev of $k_3$ with increasing $k_3$ value is a possible result of the steeper rise in $^{18}$F-fluoromisonidazole uptake that allows a more precise estimation of $k_3$. $K_1$ remained accurately estimated using shortened datasets, as observed in both patient and animal studies. As $K_1$ is predominantly determined from the early parts of TACs, the correlation between $K_1$ as calculated using full versus shortened noisy TACs was higher compared to the corresponding correlation for $k_3$ (which strongly depends on the later parts of TACs). No bias in $K_1$ or $k_3$ was observed when shortening the acquisition time, since kinetic modeling for shortened datasets was performed using truncated $mTAC_{FD}$ and $IF_{FD}$. These results indicate that $K_1$ and $k_3$ could in principle be calculated accurately from shortened acquisitions. The discrepancy between simulation and clinical results however is due to the difference in the shape of TACs as modeled using full or shortened datasets, which in turn highlights kinetic heterogeneity within tumor sub-volumes as a potential source of bias (*24,25*). When the analysis in clinical studies was repeated using $IF_{FD}$ for all datasets, the overestimation of $k_3$ was not reduced (data not shown). The potential impact of misregistration between the three $^{18}$F-fluoromisonidazole scans on overestimation of $k_3$ (by means of combining tumor regions with different pharmacokinetic properties) is a subject of an ongoing study.

Limitation of this study was the small sample size. The employed statistical methods do not address the clinical significance of the results. The clinical significance of differences between the kinetic rate constants as calculated from shortened and full dynamic PET datasets has not yet been evaluated. Further, a test-retest study will be necessary to investigate the reproducibility of $^{18}$F-fluoromisonidazole kinetic modeling.

## CONCLUSION

Using single-session 45-min shortened $^{18}$F-fluoromisonidazole dynamic PET datasets appears to be adequate for the identification of intra-tumor regions of hypoxia. However, $k_3$ was significantly overestimated in the clinical cohort. Further studies are necessary to evaluate the clinical significance of differences between the results as calculated from full and shortened datasets.

## DISCLOSURE

The authors declare no competing financial interest.


## ACKNOWLEDGEMENTS

This study was partially supported by NIH grants P30 CA008748, 5R01CA157770-04 and 5U01CA157442.

## REFERENCES


1. Horsman MR, Mortensen LS, Petersen JB, Busk M, Overgaard J. Imaging hypoxia to improve radiotherapy outcome. *Nat Rev Clin Oncol.* 2012;9:674-687.

2. Nordsmark M, Overgaard M, Overgaard J. Pretreatment oxygenation predicts radiation response in advanced squamous cell carcinoma of the head and neck. *Radiother Oncol.* 1996;41:31-39.

3. Brizel DM, Sibley GS, Prosnitz LR, Scher RL, Dewhirst MW. Tumor hypoxia adversely affects the prognosis of carcinoma of the head and neck. *Int J Radiat Oncol Biol Phys.* 1997;38:285-289.

4. Rajendran JG, Schwartz DL, O'Sullivan J, et al. Tumor hypoxia imaging with [F-18[fluoromisonidazole positron emission tomography in head and neck cancer. *Clin Cancer Res.* 2006;12:5435-5441.

5. Nordsmark M, Bentzen SM, Overgaard J. Measurement of human tumour oxygenation status by a polarographic needle electrode. An analysis of inter- and intratumour heterogeneity. *Acta Oncol.* 1994;33:383-389.

6. Russell J, Carlin SD, Burke SA, Wen B, Yang KM, Ling CC. Immunohistochemical detection of changes in tumor hypoxia. *Int J Radiat Oncol Biol Phys.* 2009;73:1177-1186.

7. Koh WJ, Rasey JS, Evans ML, et al. Imaging of hypoxia in human tumors with [F-18]fluoromisonidazole. *Int J Radiat Oncol Biol Phys.* 1992;22:199-212.

8. Rasey JS, Koh WJ, Evans ML, et al. Quantifying regional hypoxia in human tumors with positron emission tomography of [18F]fluoromisonidazole: a pretherapy study of 37 patients. *Int J Radiat Oncol Biol Phys.* 1996;36:417-428.

9. Thorwarth D, Eschmann SM, Paulsen F, Alber M. A kinetic model for dynamic [18F]-FMISO PET data to analyse tumor hypoxia. *Phys Med Biol.* 2005;50:2209-2224.

10. Wang W, Lee NY, Georgi JC, et al. Pharmacokinetic analysis of hypoxia (18)F-fluoromisonidazole dynamic PET in head and neck cancer. *J Nucl Med*. 2010;51;37-45.

11. Lim JL, Berridge MS. An efficient radiosynthesis of [18F]fluoromisonidazole. *Appl Radiat Isot. 1993*;44:1085–1091.

12. Bokacheva L, Kotedia K, Reese M, et al. Response of HT29 colorectal xenograft model to cediranib assessed with 18F-fluoromisonidazole positron emission tomography, dynamic contrast-enhanced and diffusion-weighted MRI. *NMR Biomed.* 2013;26:151-163.

13. Wang W, Georgi JC, Nehmeh SA, et al. Evaluation of a compartmental model for estimating tumor hypoxia via FMISO dynamic PET imaging. *Phys Med Biol.* 2009;54:3083-3099.

14. Rousset OG, Ma Y, Evans AC. Correction for partial volume effects in PET: principle and validation. *J Nucl Med*. 1998;39:904-911.

15. Velamuru PK, Renaut RA, Guo Hongbin, Chen K. Robust Clustering of Positron Emission Tomography Data. In *Joint Conference of the Classification Socitey of North America and Interface Foundation of North America*. 2005; St. Louis.

16. Press WH, Teukolsky SA, Wetterling WT, Flannery BP. Numerical Recipes in C. New York, NY: Cambridge University Press; 1992.

17. Passing H, Bablok W. A new biometrical procedure for testing the equality of measurements from two different analytical methods. Application of linear regression procedures for method comparison studies in clinical chemistry, Part I. *J Clin Chem Clin Biochem*. 1983;21:709-720.

18. Bland JM, Altman DG. Statistical methods for assessing agreement between two methods of clinical measurement. *Lancet*. 1986;327:307-310.

19. Zweig MH, Campbell G. Receiver-operating characteristic (ROC) plots: a fundamental evaluation tool in clinical medicine. *Clin Chem*. 1993;39:561-77.

20. Schmidtlein CR, Beattie BJ, Bailey DL, et al. Using an external gating signal to estimate noise in PET with an emphasis on tracer avid tumors. Phys Med Biol. 2010;55:6299-6326.

21. Eschmann SM, Paulsen F, Reimold M, et al. Prognostic impact of hypoxia imaging with 18F-misonidazole PET in non-small cell lung cancer and head and neck cancer before radiotherapy. *J Nucl Med.* 2005;46:253-260.

22. Thorwarth D, Eschmann SM, Scheiderbauer J, Paulsen F, Alber M. Kinetic analysis of dynamic 18F-fluoromisonidazole PET correlates with radiation treatment outcome in head-and-neck cancer. *BMC Cancer*. 2005;5:152.

23. Fleming IN, Manavaki R, Blower PJ, et al. Imaging tumour hypoxia with positron emission tomography. *Br J Cancer*. 2015;112:238-250.

24. Herholz K, Patlak CS. The influence of tissue heterogeneity on results of fitting nonlinear model equations to regional tracer uptake curves: with an application to

compartmental models used in positron emission tomography. *J Cereb Blood Flow Metab*. 1987;7:214-229.

25. Schmidt K, Lucignani G, Moresco RM, et al. Errors introduced by tissue heterogeneity in estimation of local cerebral glucose utilization with current kinetic models of the [18F]fluorodeoxyglucose method. *J Cereb Blood Flow Metab*. 1992;12:823-834.

26. Torizuka T, Nobezawa S, Momiki S, et al. Short dynamic FDG-PET imaging protocol for patients with lung cancer. *Eur J Nucl Med*. 2000;27:1538-1542.

27. Monden T, Kudomi N, Sasakawa Y, et al. Shortening the duration of [18F]FDG PET brain examination for diagnosis of brain glioma. *Mol Imaging Biol*. 2011;13:754-758.

28. Busk M, Munk OL, Jakobsen S, et al. Assessing hypoxia in animal tumor models based on pharmocokinetic analysis of dynamic FAZA PET. *Acta Oncol.* 2010;49:922-933.

**FIGURES**

**A**

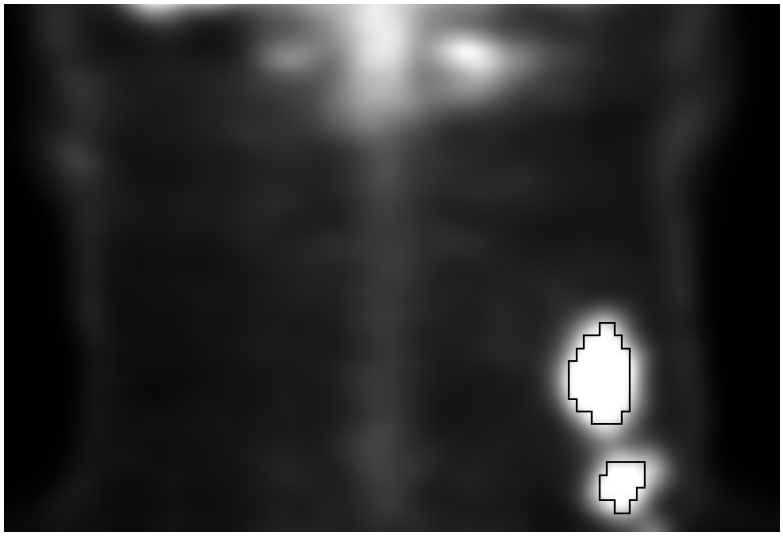

**B**

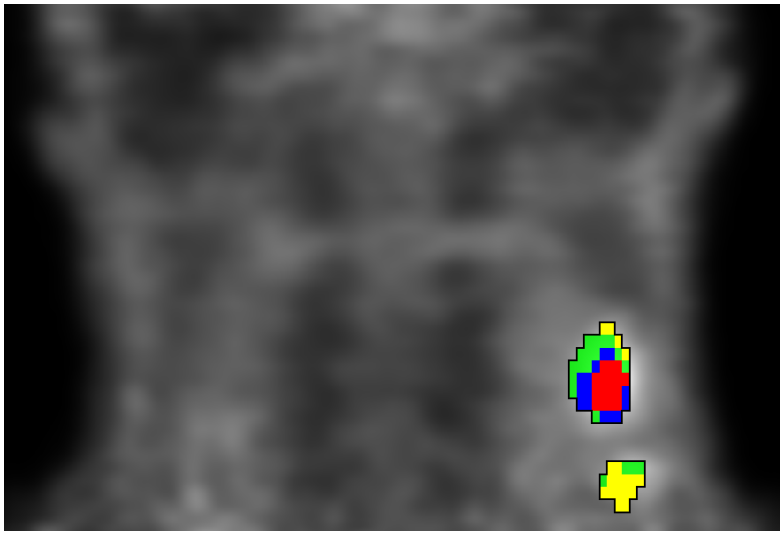

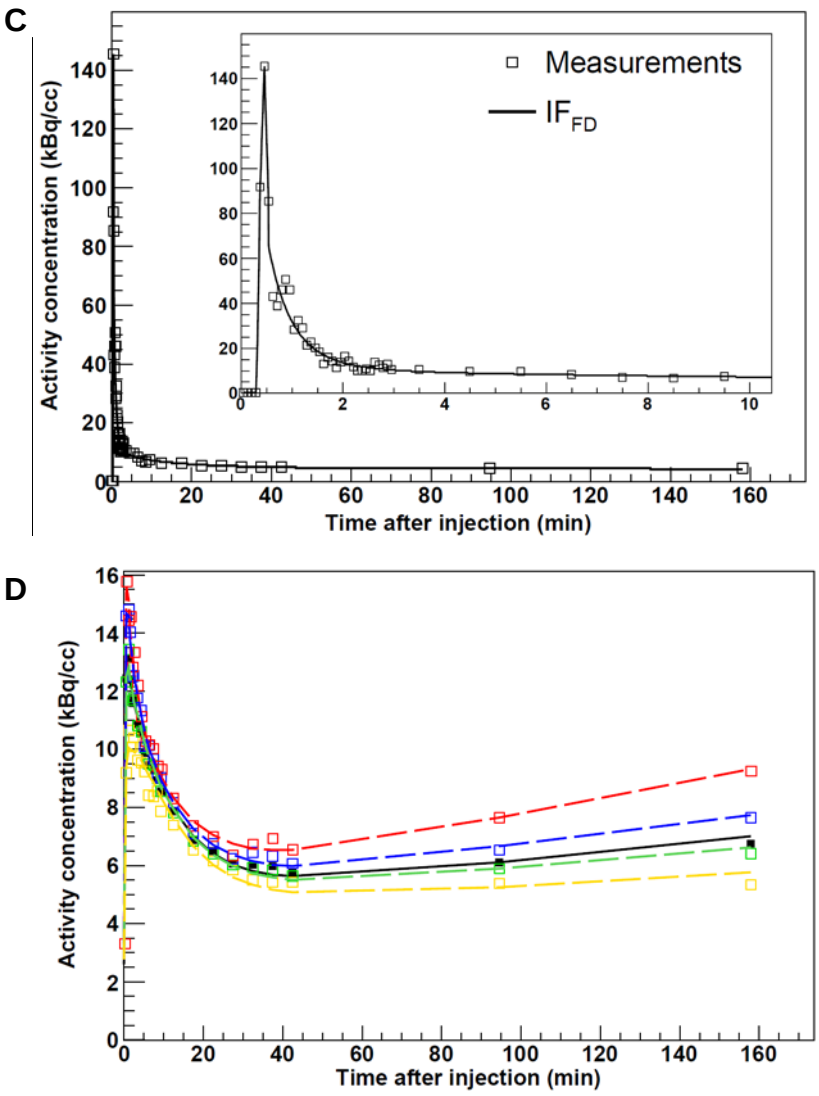


Figure 1. Clinical study of Patient #1 (lesion #1). (A) Definition of tumor volume of interest (wVOI) on the $^{18}$F-fluorodeoxyglucose PET image (coronal view). (B) wVOI is copied to a co-registered $^{18}$F-fluoromisonidazole dynamic PET image and sub-classified into 4 clusters (cVOIs). (C) Modeled input function based on the full dataset ($IF_{FD}$), superimposed on measurements. The insert shows initial 10-min of data. (D) The modeled TACs derived from wVOI (solid line) and from 4 cVOIs (dashed lines),

superimposed on the measured wVOI TAC (full squares) and cVOI TACs (empty squares). cVOIs are color-coded to those shown in (B).

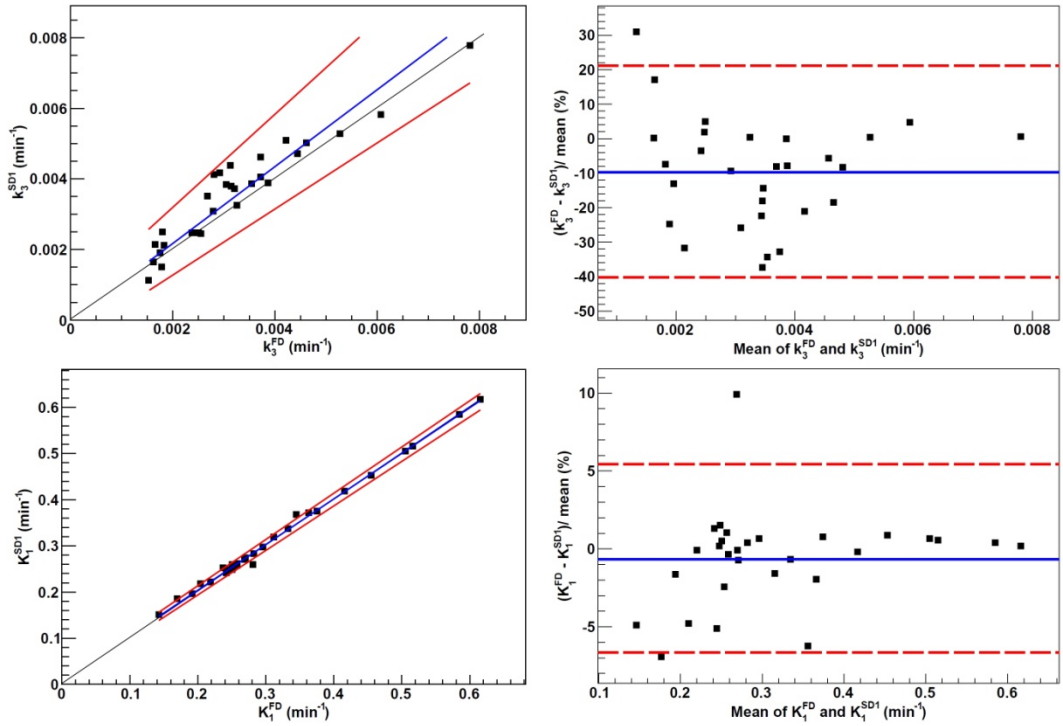


Figure 2. Passing-Bablok regression (left) and Bland-Altman analysis (right) results for $k_3$ (top) and $K_1$ (bottom), calculated using full (FD; ~170-min) and ~100-min shortened (SD1) datasets in clinical studies (n=29). Also displayed are regression line (blue) and its confidence intervals (red) for Passing-Bablok regression, and mean percentage difference (blue) with limits of agreement (red) for Bland-Altman analysis.

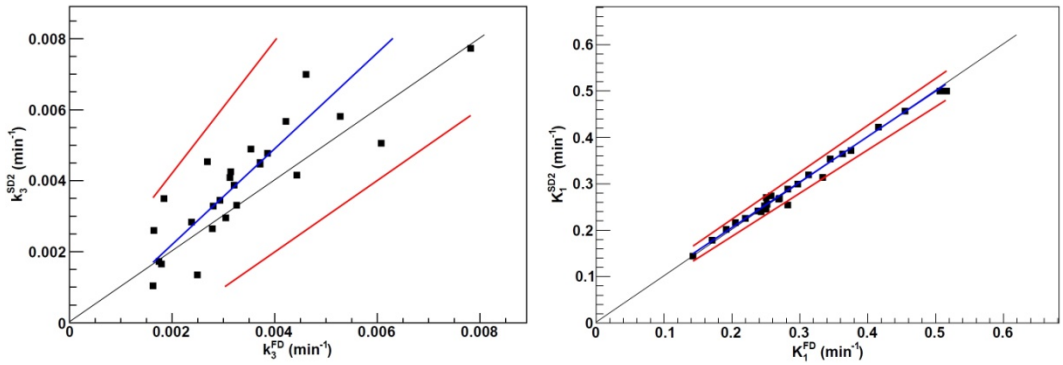


Figure 3. Passing-Bablok regression results for $k_3$ (left) and $K_1$ (right), calculated using full (FD; ~170-min) and 45-min shortened (SD2) datasets in clinical studies (n=26). Also displayed are regression line (blue) and its confidence intervals (red).

A

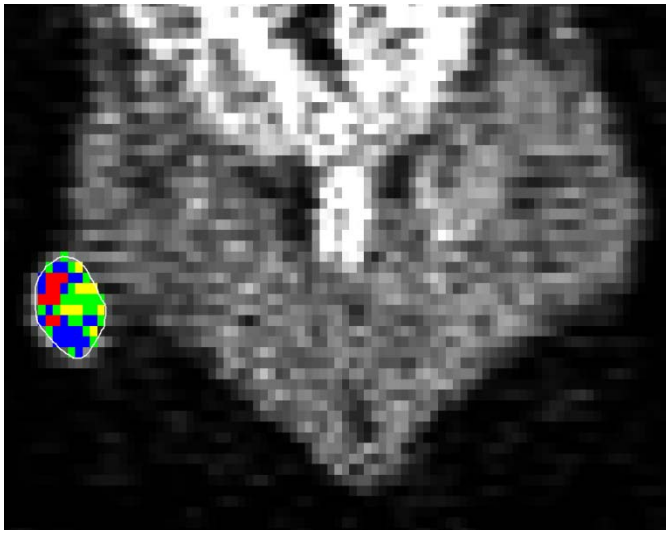

B

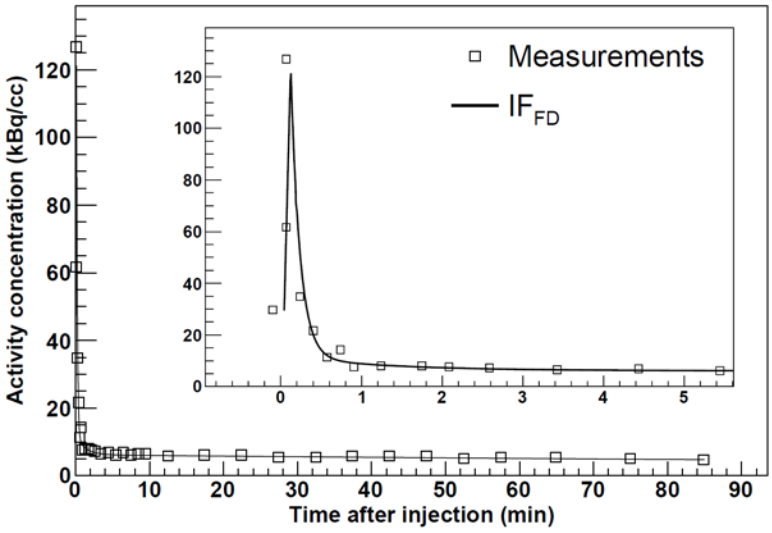
Measurements
IF$_{FD}$
Activity concentration (kBq/cc)
Time after injection (min)
0
20
40
60
80
100
120
0
10
20
30
40
50
60
70
80
90
0
1
2
3
4
5

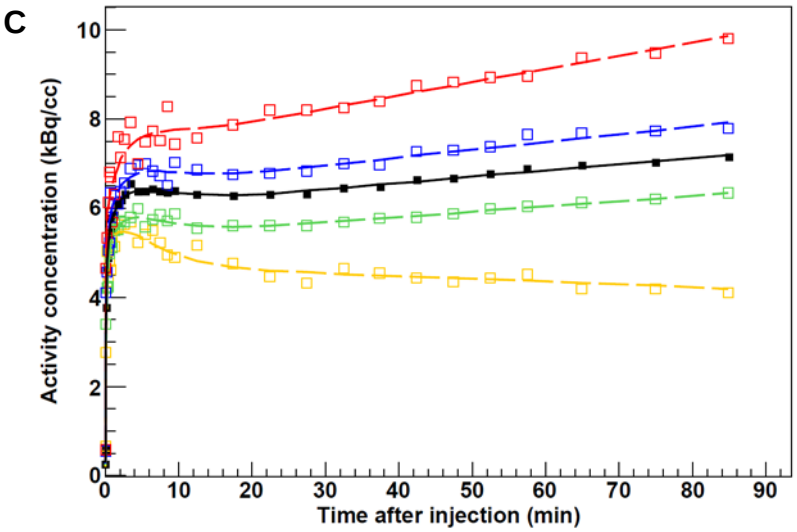


Figure 4. Kinetic modeling in tumor-bearing rodents (Animal #1). (A) Definition of the tumor volume of interest (wVOI, white contour) on the last 10-min frame of the $^{18}$F-fluoromisonidazole dynamic PET (coronal view), sub-classified into 4 clusters (cVOIs). (B) Modeled input function based on the full dataset ($IF_{FD}$), superimposed on the measured TACs. The insert shows initial 5 min of data. (C) The modeled TACs derived from wVOI (solid line) and from 4 cVOI (dashed lines), superimposed on the measured wVOI TAC (full squares) and cVOI TACs (empty squares). cVOIs are color-coded to those shown in (A).

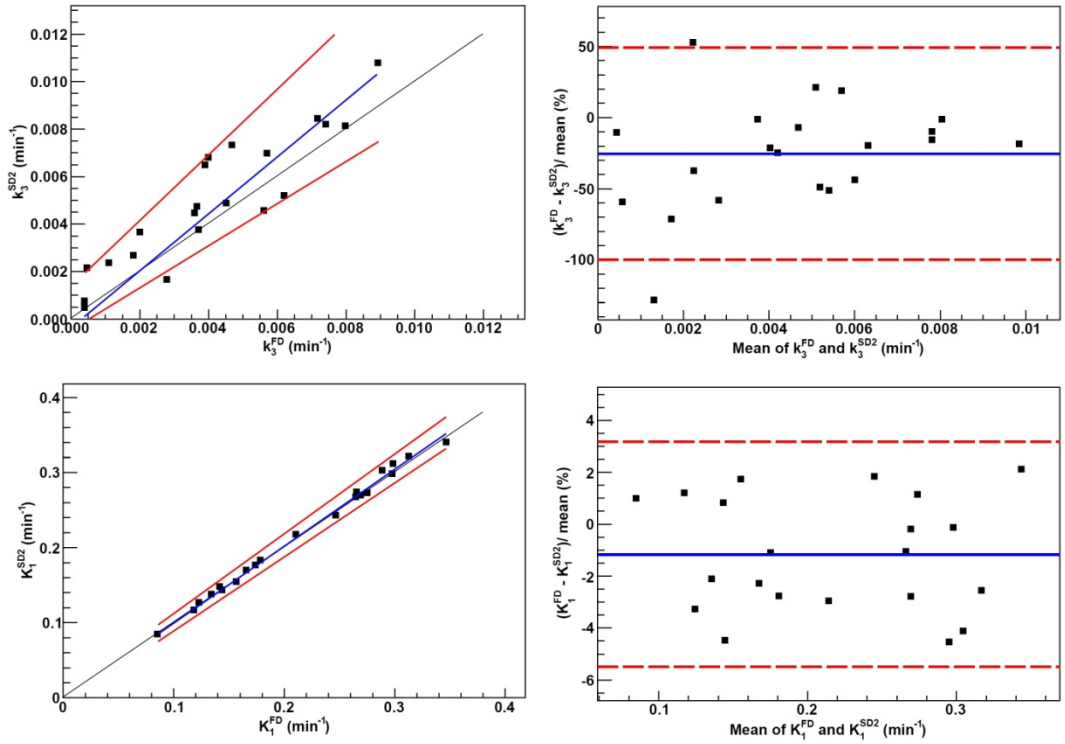


Figure 5. Passing-Bablok regression (left) and Bland-Altman analysis (right) results for $k_3$ (top) and $K_1$ (bottom), calculated using full (FD; 90-min) and 45-min shortened datasets (SD2) in preclinical studies (n=21). Also displayed are regression line (blue) and its confidence intervals (red) for Passing-Bablok regression, and mean percentage difference (blue) with limits of agreement (red) for Bland-Altman analysis.

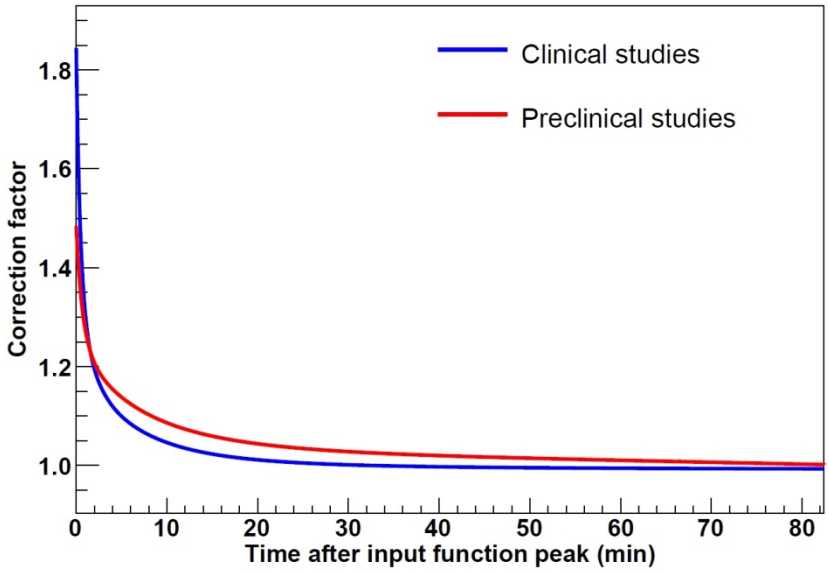


Figure 6. Correction factor for the input function due to partial volume effect, for pooled data from clinical and preclinical studies.

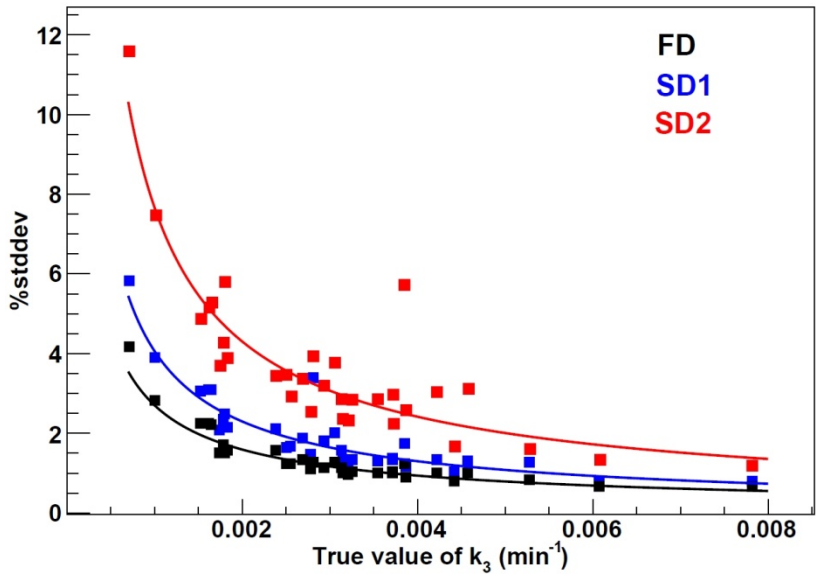


Figure 7. Percentage standard deviation in estimating $k_3$ from simulated data. FD-full dataset (~170 min), SD1-1st shortened dataset (~100-min), SD2-2nd shortened dataset (45-min).

**TABLES**

Table 1. Patient characteristics.

| Patient | Tumor stage | Tumor site | Lesion | Lesion VOI [$cm^3$] |
|---|---|---|---|---|
| 1 | cT1N2b | Left glossal tonsillar sulcus | 1 | 13.3 |
| | | and left base of tongue | 2 | 3.3 |
| 2 | T1N2b | Left tonsil | 3 | 24.2 |
| 3 | cT2N3M0 | Left tonsil | 4 | 3.3 |
| 4* | cT2N2b | Base of tongue | 5 | 32.9 |
| 5† | cT3N2a | Left tonsil and bilateral neck | 6 | 33.0 |
| | | | 7 | 6.5 |
| 6* | T2N2b | Left tonsil | 8 | 11.2 |

*Patients for whom List-mode data was not available. †Patient whose 1st $^{18}$F-fluoromisonidazole acquisition was stopped at 40 min. VOI-volume of interest.

Table 2. Summary of correlation, regression and deviation analyses.

| Dataset combination | KRC | Pearson's *r* (95% CI) | Passing-Bablok | | | | Bland-Altman | | |
|---|---|---|---|---|---|---|---|---|---|
| | | | p* | Slope (95% CI) | Intercept (95% CI) | RSD (95% CI) | p† | Mean %difference (95% CI) | 95% LOA (lower; upper) |
| FD-SD1 (clinical) n=29 | $k_3$ | 0.95 (0.89-0.98) | 0.58 | 1.08 (0.94 to 1.32) | -6.0E-6 (-6.1E-4 to 5.3E-4) | 3.4E-4 (-6.7E-4 to 6.7E-4) | 0.20 | -9.85 (-15.79 to -3.90) | -40.49; 20.80 |
| | $K_1$ | 1.00 (0.99-1.00) | 0.58 | 0.99 (0.97 to 1.00) | 0.0045 (-1.3E-4 to 0.011) | 0.0058 (-0.011 to 0.011) | 1.00 | -0.67 (-1.85 to 0.51) | -6.76; 5.42 |
| FD-SD2 (clinical) n=26 | $k_3$ | 0.85 (0.69-0.93) | 1.00 | 1.40 (1.01 to 1.86) | -6.8 E-4 (-0.0020 to 4.7E-4) | 6.3E-4 (-0.0012 to 0.0012) | Analysis not conducted | | |
| | $K_1$ | 1.00 (0.99-1.00) | 0.86 | 1.04 (0.99 to 1.08) | -0.012 (-0.024 to 2.2E-4) | 0.0060 (-0.012 to 0.012) | 1.00 | -0.30 (-1.80 to 1.19) | -7.55; 6.95 |
| FD-SD2 (preclinical) n=21 | $k_3$ | 0.91 (0.79-0.96) | 0.98 | 1.10 (0.89 to 1.38) | 5.2E-4 (-5.1E-4 to 0.0013) | 8.2E-4 (-0.0016 to 0.0016) | 0.82 | -25.77 (-43.08 to -8.44) | -100.36; 48.83 |
| | $K_1$ | 1.00 (0.99-1.00) | 0.98 | 1.02 (0.98 to 1.06) | -0.0013 (-0.0079 to 0.0069) | 0.0038 (-0.0075 to 0.0075) | 1.00 | -1.17 (-2.17 to -0.16) | -5.50; 3.16 |

*Cusum test. †Kolmogorov-Smirnov test. FD-full dataset (~170 min in clinical, 90-min in preclinical studies), SD1-1st shortened dataset (~100-min), SD2-2nd shortened dataset (45-min), CI-confidence interval, KRC-kinetic rate constant, RSD-residual standard deviation, LOA-limits of agreement.

Table 3. Summary of classification analyses.

| Dataset | KRC | AUC (95% CI) | Associated criterion |
|---|---|---|---|
| SD1 n=32 | $k_3$ | 0.70 (0.51-0.85) | >0.0021 |
| | $K_i$ | 0.91 (0.75-0.98) | >0.0027 |
| SD2 n=32 | $k_3$ | 0.80 (0.62-0.92) | >0.0034 |
| | $K_i$ | 0.86 (0.69-0.96) | >0.0023 |

SD1-1$^{st}$ shortened dataset (~100-min), SD2-2$^{nd}$ shortened dataset (45-min), AUC-area under receiver operating characteristics curve, KRC-kinetic rate constant, CI-confidence interval (binomial exact).

Table 4. Summary of simulation results.

| Kinetic rate constant | Metric | Full dataset (~170-min) | 1st shortened dataset (~100-min) | 2st shortened dataset (45-min) |
|---|---|---|---|---|
| $k_3$ | %bias | 0.0±0.1 | 0.0±0.1 | 0.0±0.2 |
| | %standard deviation | 1.4±0.7 | 2.0±1.0 | 3.7±2.0 |
| | Pearson's *r* (range) | | 0.55±0.08 (0.33-0.85) | 0.19±0.13 (0.00-0.80) |
| $K_1$ | %bias | 0.1±0.1 | 0.1±0.1 | 0.1±0.1 |
| | %standard deviation | 0.6±0.2 | 0.6±0.2 | 0.6±0.2 |
| | Pearson's *r* (range) | | 0.96±0.10 (0.43-0.99) | 0.93±0.09 (0.48-0.99) |